The scramblases VMP1 and TMEM41b are required for primitive endoderm specification by targeting WNT signaling

Markus Holzner1, Tea Sonicki1, Hugo Hunn1, Federico Uliana2,3, Weijun Jiang1, Vamshidhar R. Gade2, Karsten Weis2, Anton Wutz1#, and Giulio Di Minin1#

1 Institute of Molecular Health Sciences, Department of Biology, ETH Zurich, Zurich, Switzerland
2 Institute of Biochemistry, Department of Biology, ETH Zurich, Zurich, Switzerland
3 Current address: Johannes Gutenberg University of Mainz, 55128 Mainz, Germany
corresponding authors: awutz@ethaz.ch (AW); giulio.diminin@biol.ethz.ch (GDM)

ABSTRACT

The ER resident proteins VMP1 and TMEM41b share a conserved DedA domain, which confers lipid scramblase activity. Loss of either gene results in embryonic lethality in mice and defects in autophagy and lipid droplet metabolism. We set out to investigate their role in pluripotency and specification. For this purpose, we generated Vmp1 and Tmem41b mutations in mouse embryonic stem cells (ESCs). We observed that ESCs carrying mutations in Vmp1 and Tmem41b show robust self-renewal and an unperturbed pluripotent expression profile but accumulate LC3-positive autophagosomes and lipid droplets consistent with defects in autophagy and lipid metabolism. ESCs carrying combined mutations in Vmp1 and Tmem41b can differentiate into a wide range of embryonic cell types. However, differentiation into primitive endoderm-like cells in culture is impaired, and the establishment of extra-embryonic endoderm stem (XEN) cells is delayed. Mechanistically, we show the deregulation of genes that are associated with WNT signaling. This is further confirmed by cell surface proteome profiling, which identified a significant reduction of the WNT receptor FZD2 at the plasma membrane in Vmp1 and Tmem41b double mutant ESCs. Importantly, we show that transgenic expression of Fzd2 rescues XEN differentiation. Our findings identify the role of the lipid scramblases VMP1 and TMEM41b in WNT

signaling during extra-embryonic endoderm development and characterize their distinct and overlapping functions.

INTRODUCTION

Vesicle trafficking and membrane synthesis are intricately interconnected within cellular signaling networks. Lipid scramblases, with their property to shape lipid membrane composition, play a crucial role in facilitating inter-organelle communication. Beyond their integral involvement in maintaining cell functionality, recent studies have unveiled their implications in various pathological conditions, such as viral infection [1-5], cancer development [6-11], and inflammatory diseases [12-16]. The vacuole membrane protein 1 (VMP1) and transmembrane protein 41B (TMEM41B) are lipid scramblases with a highly conserved DedA domain [17, 18]. They localize at the ER membrane and are distinguished from other ER-associated flippases or scramblases by the property to facilitate bi-directional lipid diffusion in an ATP- and Ca2+-independent manner. VMP1 and TMEM41B are necessary for autophagosome formation [19, 20], lipid droplet metabolism [17, 21], and lipoprotein formation [22]. Additional reports proposed a more global role in ER protein homeostasis [23] and vesicle transport [24]. Despite multifaceted functions, their absence does not influence cell survival significantly. Compensatory mechanisms shared by VMP1 and TMEM41B or other ER scramblases likely maintain cellular homeostasis. While VMP1 depletion leads to a pronounced defect in autophagosome assembly [19, 20], TMEM41B appears to play a pivotal role in sustaining lipid droplet homeostasis and serves as a crucial factor in RNA virus replication [3, 25]. However, a direct comparison between the activities of VMP1 and TMEM41B has not yet been performed.

VMP1 and TMEM41B are both essential during embryonic development. Vmp1 [21] and Tmem41b [26] deficient mice die around E8.5 with a severe developmental delay. Previously, defects in the visceral endoderm function have been proposed. In particular, loss of Vmp1 has been suggested to block the synthesis and release of lipoproteins from the visceral endoderm. However, mice with defects in lipoprotein biogenesis experience mortality at a later stage, E10.5 [27, 28]. This observation

suggests a distinct and earlier involvement of VMP1 and TMEM41B in embryo development.

During implantation, the mouse embryo is composed of three lineages: the trophectoderm, the primitive endoderm (PE), and the epiblast (EPI), which is primed to develop into the embryo [29]. The EPI and PE are specified within the inner cell mass (ICM) of the blastocyst. Defects in the formation of these lineages are challenging to characterize *in vivo* as they appear pre-implantation and due to the small embryo size. To investigate the role of Vmp1 and Tmem41b in early embryonic lineage specification, we generated mutations in Vmp1 and Tmem41b in ESCs. We show that a combined Vmp1 and Tmem41b mutation in ESCs results in a specific defect in PE formation and a delayed conversion to extra-embryonic endoderm cells (XEN). This delay is caused by reduced WNT signaling and can be rescued through WNT activation.

RESULTS

Vmp1 and Tmem41b mutant ESCs accumulate LC3+ autophagosomes and lipid droplets

To assess the influence of a Vmp1 or Tmem41b depletion on mouse ESCs and in early embryo development, we engineered genomic deletions using CRISPR/Cas9 targeted mutagenesis. Vmp1 was mutated by introducing a frameshift in exon 2 (Fig.1A). Loss of Vmp1 protein was confirmed in independent mutant ESC clones ($Vmp1^{KO}$) (Fig.S1A). To abrogate Tmem41b expression, we deleted the genomic region between exons 2 and 3 (Fig.1A), which encodes the first transmembrane domain of the protein ($Tmem41b^{KO}$). This mutation is predicted to compromise the protein topology. Additionally, the splicing of exon 1 to exon 4 produces a frameshift, suggesting a null allele. The deletion was confirmed on the genomic DNA (Fig.S1B). Tmem41b mRNA levels were strongly reduced (Fig.S1C-D).

Vmp1 and Tmem41b mutant ESCs showed similar morphology (Fig.1B), proliferation (Fig.S1E), and expression of pluripotency markers (Fig.S1F-G) compared to WT ESCs. We confirmed that the pluripotency network was unchanged by a transcriptomic analysis performed in individual Vmp1 and Tmem41b mutant cells. This

analysis also showed that the transcription profile of cells was marginally affected, consistent with earlier results of ESC characterization (Fig.S1I-J and Table S2).

Considering the role of Vmp1 and Tmem41b in autophagy, we assessed the accumulation of LC3+ autophagosomes to determine the impact of their mutations. We found an increase of LC3+ puncta in both mutants compared to WT ESCs (Fig.1C and Fig.S2A-B). Interestingly, the increased frequency of LC3+ puncta was similar in Vmp1 (4X) and Tmem41b (3,5X) mutant cells. Next, mutant cells were analyzed for the retention of lipid droplets (LD). To amplify LDs, we treated all samples with oleic acid (OA) and visualized LDs by BODIPY staining. We observed that Vmp1 and Tme41b mutations led to a 4-fold increase of LD numbers with respect to WT cells (Fig.1D and Fig. S2D-E). These results suggest that both Vmp1 and Tmem41b contribute to autophagosome and lipid droplet metabolism in ESCs, recapitulating earlier studies performed in other cellular systems [17, 20]. The direct comparison of both mutations revealed a similar contribution of VMP1 and TMEM41B to both processes.

Vmp1 and Tmem41b activity is not required for ESC self-renewal

We generated double mutant cell lines to characterize potential redundant functions between VMP1 and TMEM41B. A Tmem41b mutation was engineered in Vmp1 mutant ESCs (Double KO) (Fig.S1A-D). Several independent mutant clones were obtained. Notably, Double KO cells showed a regular ESC morphology (Fig.S1H) and proliferation rate (Fig.S1E). The absence of Vmp1 and Tmem41b did not affect secretory compartments, as ER, Golgi apparatus, and late endosomes appeared normal in mutant cells (Fig.S3A). Transcriptomics analysis of Double KO cells showed a limited perturbation in gene expression (Fig.1E). The combined mutations did not result in a greater number of differentially regulated genes compared to Vmp1^{KO} cells (Fig.S3C). Minimal overlap of differentially expressed genes was detected among Vmp1, Tmem41b, and Double KO mutant cell lines (Fig.S3B-C). Additionally, we did not observe enrichment for genes associated with defined cellular processes (Fig.1F, Fig.S3D-E). The pluripotency network, as also shown by IF staining (Fig.S1F-G), was not perturbed in Double KO cells. We conclude that Vmp1 and Tmem41b are not essential for ESC self-renewal.

132 **Vmp1 and Tmem41b have redundant functions in autophagosome and lipid**
133 **droplet formations**
134 LC3 staining showed that Double KO cell lines present an exacerbated phenotype in
135 autophagosome accumulation compared to single mutants. Although the total number
136 of LC3 positive autophagosomes per cell remained unchanged (Fig.1G and Fig.S2A-
137 B), we observed an increased size. 14% of LC3 clusters in the Double KO had a larger
138 size (>3μm), compared to the 8% of autophagosomes across the single mutations and
139 3% in the WT condition (Fig.1H and Fig.S2C).
140 The simultaneous depletion of Vmp1 and Tmem41b also had a greater impact
141 on LD formation. Double KO cells showed a drastic increase of LD number in the
142 absence of oleic acid treatment, whereas in WT and Vmp1 and Tmem41b mutant
143 ESCs, LDs became detectable after OA treatment (Fig.1I-J and Fig.S2D-E). As
144 BODIPY could also stain other lipid-containing compartments, including
145 autophagosomes [30], we confirmed the enriched lipid droplets in Double KO cells by
146 refractive index tomography, which is a labelling-independent technique (Fig.1K and
147 Fig.S2F-G). Together, these results indicate that Vmp1 and Tmem41b have
148 overlapping functions in ESCs, as the combined mutation of both genes exacerbates
149 autophagosome and lipid droplet accumulation.
150
151 **Loss of Vmp1 and Tmem41b affects ESC potential to differentiate into primitive**
152 **endoderm**
153 To evaluate the effect of Vmp1 and Tmem41b on the differentiation potential of ESCs,
154 we used embryoid body (EB) differentiation (Fig.2A). After 6 days of differentiation,
155 EBs derived from WT ESCs showed increased expression of ectoderm (Sox1 and
156 Fgf5), mesoderm (Actc1 and Brachyury) and endoderm (Gata6 and Dab2) genes
157 (Fig.2B and Fig.S4A), while the expression of pluripotency markers (Nanog and
158 Pou5f1) was lost (Fig.2B and Fig.S4A). We evaluated variations in the differentiation
159 potential of mutant cells by comparing the expression of these markers by RT-qPCR.
160 For each mutant, the differentiation potential of two independent clones was tested.
161 Vmp1, Tmem41b, and double mutant ESCs formed well-defined EBs that resembled
162 those of WT cells. All cell lines efficiently differentiated into the ectoderm and
163 mesoderm lineages (Fig.2C and Fig.S4B-C). Notably, Double KO EBs showed a
164 decreased expression of the endoderm markers Dab2 (100%) and Gata6 (57% of
165 experiments) (Fig.2C and Fig.S4C). Neither single mutant showed a similar failure in

166 Dab2 expression, even if some variability was detected between the analyzed clones.
167 In the single mutants, we noticed a decreased endoderm specification, as shown by
168 Gata6 expression levels in experiments performed with Vmp1^{KO} (56% of experiments)
169 and Tmem41b^{KO} (58%) cells (Fig.2C and Fig.S4C). Our results indicate that combined
170 mutation of Vmp1 and Tmem41b leads to reduced Dab2 expression and predisposes
171 to variability in the expression of other endodermal genes.
172 We confirmed the differentiation potential of Double KO cells into ectodermal
173 lineages by generating SOX1-positive spinal cord organoids (Fig.S4D). Mesodermal
174 differentiation was inferred from the ability of double mutant EBs to form contractile
175 cardiomyocytes after plating (Video S1-2). We subsequently sectioned day 6 EBs to
176 evaluate protein expression and distribution of endoderm markers by IF. Expression
177 of GATA4, GATA6, and SOX17 was detected in all conditions but noticeably decreased
178 in Double KO compared to WT EBs (Fig.2D-E). Interestingly, decreased GATA4 and
179 GATA6 staining was pronounced in EB border regions, which resemble the primitive
180 endoderm layer [31]. In line with these findings, we confirmed the absence of DAB2 in
181 Double KO EBs (Fig.2F). DAB2 is specifically expressed in the primitive endoderm,
182 while GATA4 and GATA6 are known to be also expressed in definitive endoderm.
183 The significant reduction in both mRNA and protein levels of Dab2, along with
184 the weakened expression of endoderm markers at the edges of embryoid bodies,
185 provides evidence that the absence of Vmp1 and Tmem41b compromises the
186 formation of primitive endoderm.
187
188 **Combined Vmp1 and Tmem41b mutations delay ESC differentiation into extra-**
189 **embryonic endoderm stem (XEN) cells**
190 We tested the ability of Double KO ESCs to differentiate into extra-embryonic
191 endoderm stem (XEN) cells to characterize endodermal differentiation further. XEN
192 cells share characteristics with PE cells including cell signaling, gene expression, and
193 differentiation potential [32]. Double KO and WT cells were differentiated into XEN
194 cells with Activin A and Retinoic Acid [33]. After 6 days, WT ESCs efficiently
195 differentiated into XEN clusters (Fig.3A), exhibiting a stellate and refractile morphology
196 [33]. In Double KO cells, the formation of XEN clusters was substantially reduced. We
197 characterized XEN identity by analyzing the expression of XEN markers by RT-qPCR
198 (Fig.S5A) and immunostaining (Fig.3B and Fig.S5B). It is worth noting that the small
199 number of derived XEN cells from Double KO ESCs can be expanded for multiple

passages, as shown in Fig.S5C. This result suggests that the loss of Vmp1 and Tmem41b does not entirely prevent XEN specification, but rather causes a delay in the differentiation process.

WNT signaling is decreased in Vmp1 and Tmem41b mutant cells during XEN specification

To characterize the effect of Vmp1 and Tmem41b double mutation on XEN specification, we analyzed the transcriptomic profile of Double KO and WT cells during the differentiation process. On day two of differentiation, we detected the induction of XEN-associated genes [34] in WT cells. However, in Double KO cells these genes were weakly expressed (Fig.3C-D and Fig.S5E). Intriguingly, we did not observe any perturbation in the transcription of genes involved in lipid metabolism, autophagy, or ER maintenance (Fig.S5D).

Instead, Double KO cells show consistent deregulation of genes associated to the WNT pathway (Fig.3E-F). A close analysis of these genes allowed to identify several well-established WNT-target genes, including Dkk, Frzb, Sox17, Wnt3, and Ccdnd1 [35-38]. Their down-regulation strongly suggested a decreased activity of the WNT pathway in Double KO cells and might explain the observed defect in XEN specification [39]. Interestingly, Ddit3 was strongly upregulated in Double KO cells. DDIT3 acts as an inhibitor of the WNT signaling by repressing the transcriptional activity of the TCF7/TCF4 complex [40]. We confirmed increased levels of the DDIT3 protein in Double KO cells by Western analysis (Fig.3G) and quantified a fourfold increase over WT cells (Fig.3H). Considering that Ddit3 is not reported to be a WNT-targeted gene, but instead, its expression is controlled by VMP1 levels [41], we verified if DDIT3 increase might explain WNT-target gene repression in mutant cells. For this purpose, we depleted Ddit3 in WT and mutant cells by RNA interference. After two days of differentiation, the transcription of XEN-specific genes was evaluated by qPCR. Despite efficient siRNA-mediated reduction of Didt3 mRNA levels (Fig. 3I), we did not observe an increase in the expression of XEN marker genes in Double KO cells.

These results indicate that the increased level of DDIT3 in mutant cells is not the only cause of the XEN specification defect caused by Vmp1 and Tmem41b mutations.

234 **Vmp1 and Tmem41b mutations reduce FZD2 abundance at the plasma**
235 **membrane**

236 To identify potentially affected factors of cell signaling, we investigated the
237 influence of the Vmp1 mutation on proteins at the plasma membrane (PM) in ESCs.
238 For this purpose, we enriched surface proteins in mutant and WT cells using
239 aminooxy-biotinylation and characterized their abundance by TMT mass spectrometry
240 (Fig.S6A-B). Our analysis revealed that a limited subset of proteins showed differential
241 abundance at the plasma membrane in mutant cells, with 26 proteins significantly
242 down-regulated and 12 up-regulated (out of 1417 detected proteins) (Fig. 4A and Table
243 S4). This finding aligns with our RNA expression profiles, indicating that Vmp1 and
244 Tmem41b mutations has a limited effect on the protein levels of ESCs. It also supports
245 the conclusion that, despite defects in autophagy and lipid droplet formation, the
246 secretory pathway remains largely intact in the absence of Vmp1. GO-term analysis
247 highlighted that proteins more abundantly present at the PM in Vmp1 mutant cells are
248 characterized by an ER-Golgi localization, suggesting partial defects in retrograde
249 trafficking (Fig. 4B). Moreover, we noticed that the abundance of four GPCRs was
250 reduced at the plasma membrane of mutant cells (Fig. 4B). Among them, we found
251 the WNT-receptor FZD2 (Fig. 4A and Table S4). Other Frizzled receptors—FZD5,
252 FZD7, and FZD10— were detected at the PM but remained un-affected (Fig. 4C and
253 S6C). The decrease of FZD2 protein abundance at the PM was independent of Fzd2
254 transcription, as no difference in Fzd2 mRNA was detected between WT and mutant
255 cells (Fig. S6D).

256 To confirm these findings and assess whether FZD2 reduction contributes to
257 the XEN specification defects in Double KO cells, we generated ESCs with constitutive
258 expression of HA-Fzd2 across Vmp1KO, Double KO, and WT genotypes. We
259 evaluated HA-FZD2 translocation to the plasma membrane using a cell-impermeable
260 biotinylation reagent followed by purification of biotinylated proteins (Fig. 4D). We
261 confirmed that FZD2 is less abundant at the plasma membrane in Vmp1 mutant cells,
262 validating previous MS results (Fig. 4D-E). Notably, Double KO cells exhibited an even
263 greater reduction in FZD2 levels at the PM, suggesting an additive effect of the Vmp1
264 and Tmem41b mutations. Similar results were observed when analyzing HA-FZD2
265 enrichment at the plasma membrane in Double KO and WT cells during XEN
266 specification (Fig. 4F). In this experiment, we noticed a marked reduction of the upper

form of the FZD2 doublets in mutant cells. This suggests that FZD2 is subjected to different post-translational modifications in WT and mutant cells.

FZD2 over-expression rescues XEN differentiation defects in Vmp1 and Tmem41b mutant cells

Our observation of deregulated WNT target genes and a reduced abundance of FZD2 at the PM indicated that WNT signaling defects might impair XEN specification. To investigate if indeed the WNT signaling cascade is affected, we quantified β-CATENIN, down-stream protein, and major signal transducer of the WNT pathway. We observed a marked decrease of β-CATENIN protein in Double KO compared to WT cells (Fig. 5A). This difference was even stronger, specifically analyzing the cytoplasmic fraction of β-CATENIN that is not associated with cadherins. To explore if the defect in XEN differentiation of double mutant cells can be rescued by chemically activating WNT signaling, we employed the GSK3 kinase inhibitor (CHIR) to prevent β-CATENIN degradation. GSK3 inhibition had no effect on XEN specification in WT ESCs. However, GSK3 inhibition significantly enhanced XEN cell cluster formation in double mutant ESCs (Fig. 5B and S7A-B). Finally, to investigate whether also overexpression of FZD2 would rescue XEN differentiation defects in Double KO cells, we generated subclones with high FZD2 expression for both Double KO and WT ESCs (Fig. S7C). The increased amount of FZD2 alone did not further stimulate the WNT pathway or XEN specification in WT cells (Fig. 5C-D and S7D-F). However, FZD2 overexpression in Double KO cells was sufficient to restore their potential for differentiation into XEN cells. Collectively, our data implicate Vmp1 and Tmem41b in WNT signaling during primitive endoderm specification.

DISCUSSION

Vmp1 and Tmem41b have recently been identified in a number of genetic screens designed to study various cellular processes, including autophagy, lipid metabolism, virus maturation, and ER stress [22]. In this study, we have unveiled the role of Vmp1 and Tmem41b in regulating protein secretion. Our findings indicate that their presence is essential for the trafficking of the WNT receptor FZD2 to the plasma membrane. A drastic reduction of FZD2 in mutant cells impairs WNT signals and causes an XEN cell differentiation defect. Our data, therefore, implicate a function of Vmp1/Tmem41b in

301 WNT signaling. Given that Vmp1 expression and activity are influenced by various
302 stimuli [42, 43], the interaction between Vmp1 and Tmem41b within the secretory
303 pathway is critical for physiological and pathological processes.

304 The pleiotropic function and peculiar structure of the DedA domain found in both
305 scramblases have prompted multiple studies addressing its mode of action and role in
306 cellular homeostasis. An important point under evaluation is whether Vmp1 and
307 Tmem41b work cooperatively or show specialization for different cellular processes.
308 To address this question, we targeted Vmp1 and Tmem41b genes in ESCs and
309 introduced mutations abrogating their expression. This allowed us to directly compare
310 the specificity of Vmp1 and Tmem41b in multiple processes. We report that their
311 absence similarly affects autophagy and lipid droplet accumulation. Moreover, we
312 show that the simultaneous loss of both genes synergizes and exacerbates defects of
313 single mutants, particularly in LD formation. Notably, loss of both genes did not affect
314 self-renewal in ESCs and had only subtle effects on gene expression. Our
315 characterization shows that Vmp1 and Tmem41b perform distinct and overlapping
316 functions in ESCs. It will be interesting to understand if variating expression levels of
317 Vmp1 and Tmem41b can account for their redundancy or dominance in different
318 cellular systems.

319 The embryonic lethality caused by Vmp1 and Tmem41b mutations [21, 26]
320 during development may be explained by the defective primitive endoderm
321 specification that we detected *in vitro*. Embryoid body experiments and the direct
322 differentiation of ESCs to extra-embryonic endoderm stem (XEN) cells support a
323 specific delay in PE formation in double mutant cells. Interestingly, it has been reported
324 that other mutations leading to PE delay cause retardation and embryo lethality at E8.5
325 [44], mirroring phenotypes of Vmp1 or Tmem41b mutant embryos. While both
326 scramblases are needed in mice for regular development, the depletion of both genes
327 is required to cause a differentiation delay in ESCs. More permissive *in vitro* growth
328 conditions may explain the requirement for the depletion of both genes to manifest this
329 phenotype in cell culture. It is worth noting that single Vmp1^{KO} or Tmem41b^{KO} cells
330 also showed subtle defects in endoderm specification in embryoid bodies, albeit less
331 consistently than Double KO cells (Fig.2C). The finding of WNT signaling deregulation
332 in Vmp1 and Tmem41b XEN cells explains the specification delay detected in mutant
333 cells. This is consistent with earlier reports that the WNT/TCF7L1 transcriptional
334 response is necessary *in vitro* and *in vivo* for PE expansion [39]. Retardation – not

335 impairment – of PE specification induced by Vmp1 or Tmem41b mutations may permit
336 embryo implantation but the accumulation of defects likely blocks development during
337 gastrulation.

338 Overexpression of the FZD2 receptor rescues the defects of Vmp1 and
339 Tmem41b double mutant cells during XEN specification. We propose that the
340 decreased availability of FZD2 at the plasma membrane in mutant cells causes a delay
341 in WNT signaling activation and PE defects. The observation that Fzd2 mutant mice
342 exhibit developmental defects at later stages [45] suggests the possibility of
343 compensatory mechanisms among different Frizzled receptors *in vivo*. Future studies
344 will focus on the deep characterization of other potential GPCRs subjected to
345 Vmp1/Teme41b regulation. While our results indicate that the increased expression of
346 the WNT repressor DDIT3 alone does not fully account for the delay in XEN
347 specification, it may still contribute to this delay during embryonic development. The
348 elevated levels of DDIT3 in mutant cells might exert an additive effect, further reducing
349 WNT pathway activity.

350 Vmp1 and Tmem41b emerge as key factors in the secretary machinery of cells.
351 Beyond their established roles in lipid and membrane metabolism, we demonstrate
352 their involvement in regulating protein trafficking at the plasma membrane. Notably,
353 this effect is transcriptional independent, as evidenced by expression analyses and
354 experiments in cells with constitutive FZD2 expression. Furthermore, our findings
355 indicate that Vmp1/Tmem41b depletion does not cause a global disruption of protein
356 secretion but shows a specificity for some sub-classes of secreted proteins, such as
357 GPCRs. In denaturing conditions, the upper forms of the FZD2 protein are less
358 abundant in mutant cells. This finding suggests potential post-translational
359 modification differences between the two conditions. GPCRs are tightly regulated at
360 the ER-Golgi interface, where proper folding is essential for their route in the secretory
361 pathway. In the Golgi, GPCRs undergo extensive glycosylation, which alters their
362 molecular weight and activity. These results suggest a role of Vmp1/Tmem41b in
363 promoting the maturation and stability of a specific class of transmembrane proteins.

364 The cellular systems generated in our study will help clarify the mechanisms
365 shared by these scramblases in controlling protein secretion. Furthermore, the role of
366 Vmp1 and Tmem41b in modulating the WNT cascade may extend to other signaling
367 networks, revealing other cross-connections between cellular pathways and metabolic
368 processes.

MATERIALS AND METHODS

Cell Culture

Mouse ES cells were maintained as previously described in chemically defined 2i medium with added leukemia inhibitory factor (LIF) as described in Di Minin et al. [46]. Base media composition: DMEM (Gibco, #41965039), 15% FBS (Biowest, #S1810-500) 1% sodium pyruvate (Gibco, 11360-070), 1% non-essential amino acids (Gibco, #11140-035). Lif (2000 U/mL, homemade), PD0325901 (1 µM, AxonMedchem, #391210-10-9) and Chiron (3 µM, AxonMedchem, #252917-06-9) are added fresh before use.

EB differentiation

To obtain embryonic bodies (EBs), 200k ESCs were plated on Day1 in ESCs base media without 2i and LIF (see cell culture) into a well of a Sphericalplate5D (Kugelmeiers). On Day4, EBs have formed and are transferred to a pHEMA coated 6cm culture dish and cultured until Day6. EBs are then collected and subjected to RNA extraction and RT-qPCR analysis or prepared for sectioning and immunofluorescence. In brief, EBs are fixed in 4% PFA for 30 min, cryoprotected in 10%, 20% and 30% sucrose and then embedded and frozen in Tissue Freezing Medium (Leica, #14020108926). 15 µm sections were prepared on a cryotome, mounted onto Superfrost Plus Adhesion slides (VWR international GmBH, #631-0108) and processed for immunofluorescence staining.

Cardiomyocyte differentiation

EBs were formed as previously described. On Day4, EBs were collected and seeded onto a non-treated 10cm dish, maintaining ESC base media. Cardiomyocytes randomly specified and were observed as early as on Day6 of differentiation.

Spinal Cord Organoids (SCOs) formation

For derivation of SCOs, ESCs were plated in EBs media (DMEM- F12 (Gibco) and Neurobasal Medium (Gibco) (1:1 ratio) supplemented with 200 mM L-glutamine and 10% of Knockout serum replacement) on Sphericalplate 5D dishes (Kugelmeiers AG)

403 {Holzner, 2024 #139}. On day 2, SCOs were transferred in 10 cm tissue culture dishes
404 and treated with RA (10 nM). SCOs were collected and processed for analysis at day
405 5.
406
407 **Xen Differentiation**
408 XEN cells were obtained following a protocol by Niakan et al. with minor changes [33].
409 In brief, 230k cells were plated in XEN medium on a gelatin-coated 3cm dish. The next
410 day, the media was replaced with Xen medium containing 0.1 µM retinoic acid
411 (Thermo Fischer, #17110052) and 10 ng/mL Activin A (Peprotech, #120-14). On Day4,
412 the medium was again replaced by XEN medium, no further supplements were added,
413 and on Day6 samples were either analyzed by IF or qPCR.
414 Rescue of double KO Xen differentiation was performed by adding 1 µM Chiron
415 (AxonMedchem, #252917-06-9) at Day2, together with the retinoic acid and Activin A.
416 Media was changed on day 4 to Xen medium. XEN medium composition: RPMI 1640
417 (Gibco, #61870010), GlutaMAX^{TM} (Gibco, #61870036), 15% FBS (Biowest, #S1810-
418 500), 0,1 mM ß-mercaptoethanol (Sigma, #BCCB9882).
419
420 **CRISPR-Cas9 editing to generate mutant ESC lines**
421 Vmp1: the gRNA (gagacgcatagcaatgagta) was cloned into a px330 vector (Addgene,
422 #158973). Per 3cm well, 300k ESCs were plated and transfected with 2.5 µg of gRNA
423 containing plasmid, as well as 0.25 µg of a GFP expressing plasmid (pCMV-GFP).
424 GFP-positive cells were enriched by FACS and plated as single cells. Colonies were
425 picked. Analysis by WB was used to identify identified VMP1 KO lines. Tmem41b: the
426 gRNAs (gtatgtttgacctgggcgaa and gagtgacatgtggaaatcag) were cloned into px330
427 vectors, and KO clones were derived as described above. PCR analysis of the edited
428 locus (FW: atcttggacagggggagttc RV: gaccaggggttcattgtcatt and FW:
429 cagcacacacctttaatccagc RV: gccacatagcaagcttaagagc) identified KO clones. qPCR of
430 mRNA from Exon 2 (edited locus, N-terminal end) and Exon 7 (C-terminal end) further
431 confirmed the absence of mRNA.
432
433 **Transfection and stable cell line generation**
434 For derivation of *Fzd2*-HA ESCs the PB-HA-Fzd2-IRES-Neo plasmid [46] was used.
435 Stable expression of the construct was achieved in WT, Vmp1^{KO}, and DoubleKO ESCs
436 by co-transfection of the Piggybac and the PBase plasmids. Cells were plated by

437 limiting dilution and integration events selected with G418. Multiple clones
438 characterized by different HA-FZD2 expressions were expanded. For the
439 dowunregulation of Ddit3 the following siRNA were used. Cells were transfected with
440 Lipofectamine™ RNAiMAX Transfection Reagent.
441
442 **Proliferation assay**
443 100k ESCs were plated in a well of a MW12. 48h later, cells were collected and
444 counted. Proliferation rates were calculated as relative factor of cells collected over
445 cells seeded.
446
447 **LC3 staining and size characterization**
448 100k cells were plated on cover-slips, pre-treated with Matrigel (Corning, # 354277),
449 in N2B27 media. N2B27 composition: 50 mL Neurobasal media (Gibco, # 2348949),
450 50 mL Advanced DMEM F12 (Gibco, # 12634010), 4% BSA (Gibco, # 15260), 1% L-
451 Glutamine (Gibco, # 25030024), 1% B27 supplement (Gibco, # 2336837), 0,5% N2
452 supplement (Gibco, # 2328253), and 0,1 mM ß-mercapotethanol (Sigma,
453 #BCCB9882). The next day, samples were fixed in 4% PFA for 15 min, washed 3 times
454 with PBS and then treated with ice-cold MeOH for 5 min on RT. The staining was then
455 performed as described below. Quantification was performed with the Fiji plugin
456 TrackMate [47, 48] to automatically detect puncti with a diameter of 1, 2, and 3 microns
457 at a threshold of 600, 200 and 150, respectively. Nuclei were detected at an average
458 size of 15 microns with a threshold of 10. Unique particles were annotated for 5
459 different frames for each condition and shown as particles per cell. The experiment
460 was repeated 3 times.
461
462 **LD staining and RF microscopy**
463 Samples were plated as for the LC3 staining. For samples treated with oleic acid,
464 200 µM (Sigma-Aldrich, # O1008-1G) were added at plating, over-night. The next day,
465 samples were incubated in 5 µM BODIPY 493/503 (Invitrogen, #D3922) in PBS and
466 subsequently washed 3 times with PBS and fixed in 4 % PFA for 15 min. Samples
467 were then washed, stained with Dapi for 15 min at RT and mounted with Mowiol.
468 Quantification was performed using the Fiji plugin TrackMate [47, 48] detecting

469 droplets of 1, 2, and 3 microns in diameter at a threshold of 900. Nuclei were detected
470 at 10 micron and a threshold of 1.
471 For RF microscopy, 250k cells were plated per well of a 6 well glass bottom plate
472 (Cellvis, # P06-1.5H-N) in N2B27 media. After 36 h samples were treated with 200 µM
473 oleic acid o/n and then with BODIPY for 3 h. Samples were washed 3 times with PBS
474 and maintained in N2B27 for RF microscopy. The imaging was performed on
475 Tomocube HT-X1 instrument at 37C and 5 % CO2. At least 5-8 images were acquired
476 for each condition for each well. The z-stacks were acquired with 1.06 µm slices. Max
477 Intensity projections (MIP) are generated on the Tomostudio 3.3.9. The fluorescence
478 max intensity projections were resized to Refractive index tomograms for comparison.
479 The ROIs from each image were isolated for further analysis. Comdet plugin was used
480 for identifying high refractive index regions. The approximate particle size was 2 pixels
481 and Intensity threshold values were chosen individually for each image to avoid any
482 false positives or negatives.
483
484 **Immunofluorescence**
485 Samples were washed 3 times with PBS, fixed in 4% PFA for 10 min and again washed
486 3 times with PBS. Samples stained for LC3 were then treated for 5 min with 100%
487 MeOH at RT and washed again 3 times with PBS. Samples were then blocked and
488 permeabilized with 10% donkey serum (Jackson Immunoresearch, #017-000-121)
489 and 0,1% Triton X (Thermo Fischer, # HFH10) in PBS for 20 min and incubated with
490 primary antibodies at 4 °C over-night. Oct4 (1:100, Satna Cruz, # sc-5279), Nanog
491 (1:100, Abcam, # ab80892), Sox2 (1:50, R&D Systems #AF2018), Lc3 (1:200, Cell
492 Signalling, # 2775S), Pdi (1:200, Cell Signalling, # 3501S), Rcas1 (1:200, Cell
493 Signalling, # 12290S), Rab7 (1:200, Cell Signaling, # 9367S) Sox1 (1:50, R&D
494 Systems, # AF3369), Sox17 (1:200 R&D Systems, # AF1924-SP), Gata4 (1:100 R&D
495 Systems, # AF1700-SP), Gata6 (1:100 R&D Systems, # AF1700-SP), Dab2 (1:100
496 BD, # 610464). The next day, samples were washed 3 times with 0.1% Triton X in PBS
497 and then incubated with secondary antibodies and Dapi.
498
499 **Western Blot Analysis**
500 Cells were lysed in membrane buffer (150 mM NaCl, 50 mM Tris-HCl pH 7,5, 1 mM 2-
501 mercaptoethanol (Sigma, #M3148) and 1% CHAPS (Sigma, #C3023) in water).
502 Lysates were run on SDS-Page and transferred to nitrocellulose membranes. Bands

were detected with the Amersham ECL Prime Western Blotting Detection Reagents (#RPN2232) and captured on Fujifilm Super RX-N films (#47410). Antibodies for Vmp1 (Cell Signalling, #12929S) ,DDIT3 (Cell Signalling, #2895T), β-CATENIN (Santa Cruz, sc-7963), β-ACTIN (BioLegend, W16197A), E-CADHERIN (BioLegend, 67A4), H3 (Abcam, #1791), HA-epitope (Roche, 11867423001), HSP90 (Santa Cruz, #sc-101494) were used. The Quantification of western blot bands was performed with ImageJ.

RNA extraction and RT qPCR

RNA was extracted with the RNeasy Kit (Quiagen, #74104) following the manufacturer's instructions, including the on-column DNA digestion. EB and SCO samples were pre-treated with the QIAshredder (Quiagen, #79656). cDNAs were prepared using the Bio-Rad iScript Reverse Transcription Supermix for RT-qPCR (#1708841). RT qPCR samples were prepared using the KAPPA SYBR R fast (Roche, KK4611). Primer Sequences:

Tmem41b Exon2 FW: TGCAGAAGCTGGATCAGCAA, RV: GAGCCTTGGCGTCATCCATA

Tmem41b Exon7 FW: GCAGGTAGAGCGTCACAGAG, RV: TGCAGAGTTGTTCCTGCCTT

Sdha FW: CGTTATGTGAGGGGTGTGCCTT, RV: CCTTACCAAACCTTGTGTCTGGA

Sox1 FW: ACGTAGCCAACGTAGACAC, RV: ATGAGCGTCGTCCCGTGG

Fgf5 FW: GCCTGTCCTTGCTCTTCCTCAT, RV: GGAGAAGCTGCGACTGGTGA

Actc1 FW: TGTAGGACCGTGTCGAAACC, RV: CGAAACCACACACTGTTACCG

Brachyury FW: TCTCTGGTCTGTGAGCAATGGT, RV: TGCGTCAGTGGTGTGTAATGTG

Gata6 FW: GAAGCGCGTGCCTTCATC, RV: GTAGTGGTTGTGGTGTGACAGTTG

Dab2 FW: TTGATGATGTGCCTGATGCT, RV: TTTGCTTGTGTTGTCCCTGA

Sox17 FW: CCCAACACTCCTCCCAAAGTATC, RV: TTCCCTGTCTTGGTTGATTTCT

Ddit3 FW: GGCTCAAGCAGGAAATCGAG, RV: AAGTGAGAGGCTGTTGACAC

Quantification and statistical analysis

537 Statistical analysis was performed using Python and GraphPad Prism. Data are
538 presented as mean-centered and the standard deviation. All experiments were
539 repeated with at least 3 independent biological replicates, unless stated otherwise.
540 The statistical test used to evaluate significance is the Welch's *t* test. Statistical
541 significance in the figures is denoted as follows: ns: $p > 0.05$, *: $p < 0.05$, **: $p < 0.01$,
542 ***: $p < 0.001$.
543
544 **RNA seq**
545 RNA samples were submitted to the Functional Genomics Center in Zurich (FGCZ) for
546 RNA sequencing. The quality of the RNA was determined with a Fragment Analyzer
547 standard sensitivity RNA measurement (SS RNA kit (15 nt), Agilent, Waldbronn,
548 Germany). The measured concentrations (> 50 ng/µl) and RIN (>9.9) values qualified
549 for a Poly-A enrichment strategy in order to generate the sequencing libraries applying
550 the TruSeq mRNA Stranded Library Prep Kit (Illumina, Inc, California, USA). After Poly-
551 A selection using Oligo-dT beads the mRNA was reverse-transcribed into cDNA. The
552 cDNA was fragmented, end-repaired and polyadenylated before ligation of TruSeq UD
553 Indices (IDT, Coralville, Iowa, USA). The quality and quantity of the amplified
554 sequencing libraries were validated using a Fragment Analyzer SS NGS Fragment Kit
555 (1–6000 bp) (Agilent, Waldbronn, Germany). The equimolar pool of samples was
556 spiked into a NovaSeq6000 run targeting 20M reads per sample on a S1 FlowCell
557 (Novaseq S1 Reagent Kit, 100 cycles, Illumina, Inc, California, USA). Reads from
558 RNA-seq were first preprocessed by Trimmomatic (v0.40) [49] to remove low-quality
559 bases and adapters. Then, reads were aligned to mouse genome GRCm38 (release
560 81 version from Ensembl) using HISAT2 (v2.2.1) [50]. HTSeq Count (v2.0.2) [51] was
561 used to count reads for each gene (Ensembl GRCm38.81), ignoring reads on
562 overlapped regions. Differentially expressed genes were defined by DESeq2 (v1.40.2)
563 [52]. MA plot was generated using custom-made scripts. Genes significantly enriched
564 show a fold change > 1 and FDR (adjusted p-value) < 0.01. The read counts were
565 transformed in RPKM for the heatmap representations of specific genes and
566 pathways. The genes corresponding to germ-layer differentiation markers (including
567 those for embryonic and extra-embryonic endoderm), biological processes, and
568 signaling pathways were obtained through literature mining and the KEGG database
569 (Table S1). The processed data are available as excel files (Table S2 and Table S3)

570 and raw data have been deposited on NCBI SRA database under the accession:
571 PRJNA1031567
572
573 ***Surface Proteome Profiling***
574 Sample preparation and biotin labelling was performed following the instructions from
575 {Wojdyla, 2020 #140}{Weekes, 2012 #141}. In brief, 10M cells were collected per
576 sample using Accutase (Biolegend, #423201). Cell pellets were washed one with PBS
577 and then incubated, resuspended in 1 mL biotinylation buffer (97 µM aminooxy-biotin,
578 Biotium #90113, 1 mM sodium periodate, Thermo-scientific #20504, 0,093% aniline,
579 Sigma-Aldrich, #242284) for 30 min at 4 °C. Next, cells were pelleted, the reaction
580 quenched with 1 mM glycerol (30min, 4 °C) and washed once with PBS and lysed in
581 1 mL of lysis buffer (see western blot) by sonication (Dr. Hielscher sonicator, 30 sec at
582 80% amplitude and 80% cycle time). Lysates were pelleted, the supernatant
583 transferred into a fresh tube and incubated with 30 µL (dry resin) of streptavidin
584 agarose resin (Thermo-Scientific, #20347) for 1.5h at 4 °C. beads collected,
585 transferred onto a column (BioRad, #7326008) and washed with 8 mL of lysis buffer
586 and 4 mL of 0,5% SDS in 50 mM TEAB. Beads were resuspended in 200 µL 50 mM
587 Ambic with 10 mM TCEP (30 min, 37 °C), then 20 mM iodoacetamide was added (30
588 min. 37 °C). Beads were further washed with 4 mL of SDS buffer (see above), 8 mL
589 Urea buffer (6M Urea in 50 mM TEAB, pH=8,5), and with 2 mL 50 mM TEAB. Beads
590 were taken up in 200 µL TEAB buffer and digested with 3 µL Trypsin (Promega) over
591 night, 37 C. Tryptic digestion was quenched by the addition of acetonitrile (ACN).
592 Tandem mass tag (TMT) isobaric reagents (TMTpro 6plex Thermo Fisher Scientific)
593 were dissolved in anhydrous ACN to a final concentration of 20 mg/ml, of which a
594 unique TMT label was added (100µg). Peptides were incubated at room temperature
595 for one hour, TMT labeling reactions were halted by 0.3% hydroxylamine and dried.
596 Peptides were fractionated by high pH fraction in reverse phase (microspin column,
597 Nest group) following the procedure based on the high pH reversed-phase peptide
598 fractionation kit (Pierce).
599
600 LC-MS/MS was performed on an Orbitrap Exploris 480 mass spectrometer (Thermo
601 Fisher) coupled to an Vanquish Neo liquid chromatography system (Thermo Fisher).
602 Peptides were separated using a reverse phase column (75 µm ID x 400 mm New
603 Objective, in-house packed with ReproSil Gold 120 C18, 1.9 µm, Dr. Maisch GmbH)

across 180 min linear gradient from 7 to 35% (buffer A: 0.1% [v/v] formic acid; buffer B: 0.1% [v/v] formic acid, 80% [v/v] acetonitrile). Samples were acquired in DDA mode (Data Dependent Acquision) with MS1 scan (scan range = 350-1500, R=120K, max injection time auto and AGC target = 100), followed by dependent MS2 scans (first mass (m/z) 110, R = 45K, max injection time auto and AGC target = 200).Cycle time was set to 2 sec. Peptides with charge between 2-5 were isolated (m/z = 0.7) and fragmented (NCE 36%).

Acquired spectra were searched using the MaxQuant software version 2.1.0.0 against mus musculus proteome reference dataset (http://www.uniprot.org/, downloaded on 03.04.2020) extended with reverse decoy sequences. The search parameters were set to tryptic peptides, maximum two missed cleavage, carbamidomethyl as static peptide modification, oxidation (M) and deamidation (N-terminal) and TMT6 as static peptide modification. The MS and MS/MS mass tolerance was set to 10 ppm. False discovery rate of < 1% was used at PSM and protein level. Abundance of 1417 proteins was determined from the intensity of top two peptides. Intensities values were median normalized and missing values were imputed using random sampling from a normal distribution generated from 1% less intense values. Statistical analysis was performed using unpaired two sided t-test and pvalues were corrected using Benjamin-Hochberg correction. The entire dataset, including raw data, generated tables and scripts used for the data analysis are available in the PRIDE repository: PXD053039. Matrices with protein intensities are reported in Table S4.

Competing interest

The authors declare no competing interests.

Acknowledgments

We acknowledge the Functional Genomics Center Zurich (FGCZ) for technical support and Sungsik Lee from ScopeM facility for help on the RF microscopy. We thank G.J. Pereira, C. Fimiani, and U. Sutter for their help with reagents. We thank C. Ciaudo, A. Grison, J. Corn, and K. Basler for their helpful discussions. GDM was supported by the ETH Zurich Postdoctoral Fellowship Program as well as the Marie Curie Actions

for People COFUND Program. This work was supported by grants from the Swiss National Science Foundation (SNF grants 31003A_152814/1 and 31003A_175643/1).

Author Contributions

Conceptualization: MH, AW and GDM; Data curation: MH, FU, VG and GDM; Formal analysis: MH, TS, HH, FU, VG, and GDM; Funding acquisition: KW, AW and GDM; Investigation: MH, AW and GDM; Methodology: MH, TS, HH, FU, VG, WJ, and GDM; Project administration: AW, GDM; Resources: MH, KW, AW and GDM; Supervision: KW, AW and GDM; Validation: MH, GDM; Visualization: MH, FU, VG and GDM; Writing – original draft: MH, AW and GDM; Writing – review & editing: MH, TS, HH, FU, VG, WJ, KW, AW and GDM.

REFERENCES

1. Trimarco, J.D., et al., *TMEM41B is a host factor required for the replication of diverse coronaviruses including SARS-CoV-2.* PLoS Pathog, 2021. **17**(5): p. e1009599.
2. Sun, L., et al., *Genome-scale CRISPR screen identifies TMEM41B as a multi-function host factor required for coronavirus replication.* PLoS Pathog, 2021. **17**(12): p. e1010113.
3. Hoffmann, H.H., et al., *TMEM41B Is a Pan-flavivirus Host Factor.* Cell, 2021. **184**(1): p. 133-148 e20.
4. Kratzel, A., et al., *A genome-wide CRISPR screen identifies interactors of the autophagy pathway as conserved coronavirus targets.* PLoS Biol, 2021. **19**(12): p. e3001490.
5. Baggen, J., et al., *Cellular host factors for SARS-CoV-2 infection.* Nat Microbiol, 2021. **6**(10): p. 1219-1232.
6. Lin, W., et al., *VMP1, a novel prognostic biomarker, contributes to glioma development by regulating autophagy.* J Neuroinflammation, 2021. **18**(1): p. 165.
7. Ropolo, A., et al., *A Novel E2F1-EP300-VMP1 Pathway Mediates Gemcitabine-Induced Autophagy in Pancreatic Cancer Cells Carrying Oncogenic KRAS.* Front Endocrinol (Lausanne), 2020. **11**: p. 411.
8. Folkerts, H., et al., *Elevated VMP1 expression in acute myeloid leukemia amplifies autophagy and is protective against venetoclax-induced apoptosis.* Cell Death Dis, 2019. **10**(6): p. 421.
9. Rodriguez, M.E., et al., *A novel HIF-1alpha/VMP1-autophagic pathway induces resistance to photodynamic therapy in colon cancer cells.* Photochem Photobiol Sci, 2017. **16**(11): p. 1631-1642.
10. Gilabert, M., et al., *Novel role of VMP1 as modifier of the pancreatic tumor cell response to chemotherapeutic drugs.* J Cell Physiol, 2013. **228**(9): p. 1834-43.

677 11. Guo, L., et al., *Novel roles of Vmp1: inhibition metastasis and proliferation of*
678 *hepatocellular carcinoma.* Cancer Sci, 2012. **103**(12): p. 2110-9.
679 12. Zack, S.R., et al., *Vacuole Membrane Protein 1 (VMP1) Restricts NLRP3 Inflammasome*
680 *Activation by Modulating SERCA Activity and Autophagy.* Res Sq, 2023.
681 13. Yao, Y., et al., *WHSC1L1-mediated epigenetic downregulation of VMP1 participates in*
682 *herpes simplex virus 1 infection-induced mitophagy impairment and*
683 *neuroinflammation.* Mol Immunol, 2023. **163**: p. 63-74.
684 14. Li, X.Q., et al., *TMEM41B Is an Interferon-Stimulated Gene That Promotes Pseudorabies*
685 *Virus Replication.* J Virol, 2023. **97**(6): p. e0041223.
686 15. Loncle, C., et al., *The pancreatitis-associated protein VMP1, a key regulator of inducible*
687 *autophagy, promotes Kras(G12D)-mediated pancreatic cancer initiation.* Cell Death
688 Dis, 2016. **7**(7): p. e2295.
689 16. Jiang, X., et al., *Lack of VMP1 impairs hepatic lipoprotein secretion and promotes non-*
690 *alcoholic steatohepatitis.* J Hepatol, 2022. **77**(3): p. 619-631.
691 17. Li, Y.E., et al., *TMEM41B and VMP1 are scramblases and regulate the distribution of*
692 *cholesterol and phosphatidylserine.* J Cell Biol, 2021. **220**(6).
693 18. Ghanbarpour, A., et al., *A model for a partnership of lipid transfer proteins and*
694 *scramblases in membrane expansion and organelle biogenesis.* Proc Natl Acad Sci U S
695 A, 2021. **118**(16).
696 19. Molejon, M.I., et al., *The VMP1-Beclin 1 interaction regulates autophagy induction.* Sci
697 Rep, 2013. **3**: p. 1055.
698 20. Moretti, F., et al., *TMEM41B is a novel regulator of autophagy and lipid mobilization.*
699 EMBO Rep, 2018. **19**(9).
700 21. Morishita, H., et al., *A critical role of VMP1 in lipoprotein secretion.* Elife, 2019. **8**.
701 22. Hama, Y., H. Morishita, and N. Mizushima, *Regulation of ER-derived membrane*
702 *dynamics by the DedA domain-containing proteins VMP1 and TMEM41B.* EMBO Rep,
703 2022. **23**(2): p. e53894.
704 23. Tornero-Ecija, A., et al., *A Dictyostelium model for BPAN disease reveals a functional*
705 *relationship between the WDR45/WIPI4 homolog Wdr45l and Vmp1 in the regulation*
706 *of autophagy-associated PtdIns3P and ER stress.* Autophagy, 2022. **18**(3): p. 661-677.
707 24. Bard, F., et al., *Functional genomics reveals genes involved in protein secretion and*
708 *Golgi organization.* Nature, 2006. **439**(7076): p. 604-7.
709 25. Huang, D., et al., *TMEM41B acts as an ER scramblase required for lipoprotein*
710 *biogenesis and lipid homeostasis.* Cell Metab, 2021. **33**(8): p. 1655-1670 e8.
711 26. Van Alstyne, M., et al., *Stasimon/Tmem41b localizes to mitochondria-associated ER*
712 *membranes and is essential for mouse embryonic development.* Biochem Biophys Res
713 Commun, 2018. **506**(3): p. 463-470.
714 27. Farese, R.V., Jr., et al., *Knockout of the mouse apolipoprotein B gene results in*
715 *embryonic lethality in homozygotes and protection against diet-induced*
716 *hypercholesterolemia in heterozygotes.* Proc Natl Acad Sci U S A, 1995. **92**(5): p. 1774-
717 8.
718 28. Raabe, M., et al., *Knockout of the abetalipoproteinemia gene in mice: reduced*
719 *lipoprotein secretion in heterozygotes and embryonic lethality in homozygotes.* Proc
720 Natl Acad Sci U S A, 1998. **95**(15): p. 8686-91.
721 29. Arnold, S.J. and E.J. Robertson, *Making a commitment: cell lineage allocation and axis*
722 *patterning in the early mouse embryo.* Nat Rev Mol Cell Biol, 2009. **10**(2): p. 91-103.

30. O'Rourke, E.J., et al., *C. elegans major fats are stored in vesicles distinct from lysosome-related organelles.* Cell Metab, 2009. **10**(5): p. 430-5.
31. Zeevaert, K., et al., *Cell Mechanics in Embryoid Bodies.* Cells, 2020. **9**(10).
32. Kruithof-de Julio, M., et al., *Regulation of extra-embryonic endoderm stem cell differentiation by Nodal and Cripto signaling.* Development, 2011. **138**(18): p. 3885-95.
33. Niakan, K.K., et al., *Derivation of extraembryonic endoderm stem (XEN) cells from mouse embryos and embryonic stem cells.* Nat Protoc, 2013. **8**(6): p. 1028-41.
34. Ngondo, R.P., et al., *Argonaute 2 Is Required for Extra-embryonic Endoderm Differentiation of Mouse Embryonic Stem Cells.* Stem Cell Reports, 2018. **10**(2): p. 461-476.
35. Tetsu, O. and F. McCormick, *Beta-catenin regulates expression of cyclin D1 in colon carcinoma cells.* Nature, 1999. **398**(6726): p. 422-6.
36. Du, Y.C., et al., *Induction and down-regulation of Sox17 and its possible roles during the course of gastrointestinal tumorigenesis.* Gastroenterology, 2009. **137**(4): p. 1346-57.
37. Zhang, Z., et al., *Secreted frizzled related protein 2 protects cells from apoptosis by blocking the effect of canonical Wnt3a.* J Mol Cell Cardiol, 2009. **46**(3): p. 370-7.
38. Aguilera, O., et al., *The Wnt antagonist DICKKOPF-1 gene is induced by 1alpha,25-dihydroxyvitamin D3 associated to the differentiation of human colon cancer cells.* Carcinogenesis, 2007. **28**(9): p. 1877-84.
39. Athanasouli, P., et al., *The Wnt/TCF7L1 transcriptional repressor axis drives primitive endoderm formation by antagonizing naive and formative pluripotency.* Nat Commun, 2023. **14**(1): p. 1210.
40. Chiu, C.S., et al., *Exploiting Honokiol-induced ER stress CHOP activation inhibits the growth and metastasis of melanoma by suppressing the MITF and beta-catenin pathways.* Cancer Lett, 2019. **442**: p. 113-125.
41. Wang, S., et al., *Loss of acinar cell VMP1 triggers spontaneous pancreatitis in mice.* Autophagy, 2022. **18**(7): p. 1572-1582.
42. Wang, C., et al., *An autoregulatory feedback loop of miR-21/VMP1 is responsible for the abnormal expression of miR-21 in colorectal cancer cells.* Cell Death Dis, 2020. **11**(12): p. 1067.
43. Lo Re, A.E., et al., *Novel AKT1-GLI3-VMP1 pathway mediates KRAS oncogene-induced autophagy in cancer cells.* J Biol Chem, 2012. **287**(30): p. 25325-34.
44. Futterer, A., et al., *Ablation of Dido3 compromises lineage commitment of stem cells in vitro and during early embryonic development.* Cell Death Differ, 2012. **19**(1): p. 132-43.
45. Yu, H., et al., *Frizzled 1 and frizzled 2 genes function in palate, ventricular septum and neural tube closure: general implications for tissue fusion processes.* Development, 2010. **137**(21): p. 3707-17.
46. Di Minin, G., et al., *TMED2 binding restricts SMO to the ER and Golgi compartments.* PLoS Biol, 2022. **20**(3): p. e3001596.
47. Ershov, D., et al., *TrackMate 7: integrating state-of-the-art segmentation algorithms into tracking pipelines.* Nat Methods, 2022. **19**(7): p. 829-832.
48. Tinevez, J.Y., et al., *TrackMate: An open and extensible platform for single-particle tracking.* Methods, 2017. **115**: p. 80-90.

49. Bolger, A.M., M. Lohse, and B. Usadel, *Trimmomatic: a flexible trimmer for Illumina sequence data.* Bioinformatics, 2014. **30**(15): p. 2114-20.
50. Kim, D., et al., *Graph-based genome alignment and genotyping with HISAT2 and HISAT-genotype.* Nat Biotechnol, 2019. **37**(8): p. 907-915.
51. Putri, G.H., et al., *Analysing high-throughput sequencing data in Python with HTSeq 2.0.* Bioinformatics, 2022. **38**(10): p. 2943-2945.
52. Love, M.I., W. Huber, and S. Anders, *Moderated estimation of fold change and dispersion for RNA-seq data with DESeq2.* Genome Biol, 2014. **15**(12): p. 550.

FIGURE LEGENDS

Figure 1. Vmp1 and Tmem41b double KO ESCs display increased autophagosome and lipid droplet accumulation

(A) Schematic representation of the CRISPR/Cas9-mediated KO strategy for Vmp1 and Tmem41b genes. For depleting Vmp1 (top) a single gRNA inducing an indel mutation has been used. In the case of the Tmem41b gene (bottom), two gRNAs were used to delete exons 2 and 3. The sequences coding for transmembrane domains (TM) are indicated in blue, the conserved DedA domain is highlighted in yellow, red lines indicate cut sites of gRNAs. **(B)** Colony morphology of $VMP1^{KO}$ and $Tmem41^{KO}$ ESCs remains unchanged compared to WT ESCs. Scale bar: 100 µm. **(C)** VMP1 and Tmem41b depletion induce accumulation of autophagosomes in ESCs. The graph shows the quantification of LC3 puncta per cell of a representative experiment (see Fig.S2A). Data were collected from more than 200 cells. For each KO condition, two independent clones have been analyzed. Dots correspond to the frames analyzed per sample. Data are represented as mean ± SD. The P-value is relative to the WT sample. **(D)** Vmp1 and Tmem41b depletion leads to the accumulation of lipid droplets (LD) in ESCs. Graph quantifies LD per cell in WT and KO ESCs (see Fig.S2D). ± oleic acid treatment. At least 500 cells were analyzed for every condition; dots represent independent biological replicates. Data are represented as mean ± SD. (**E-G)** Transcriptional analysis of Double KO ESCs did not identify many deregulated genes. **(E)** Shown are differentially regulated genes in Double KO ESCS in blue as MA plot. Genes highlighted in red are pluripotency markers. **(F)** Differentially regulated genes do not cluster in essential processes. The graph shows differentially expressed genes of single and double KO ESCs by cellular processes. Dot size correlates to the number of deregulated genes within a cellular process. **(G-H)** Double KO ESCs accumulate LC3+ autophagosomes of increased size. **(G)** Shown are representative IF images of WT and double KO ESCs stained for LC3. Nuclei are stained with Dapi. Scale bar: 20 µm. **(H)** Plotted is the quantification of LC3 puncta of 3 µm in diameter. For each condition, two independent clones have been analyzed. Dots correspond to the frames analyzed per sample. Data were collected from more than 200 cells. Data are represented as mean ± SD. The P-value is relative to the Double KO sample with the highest SD. **(I-J)** Double KO ESCs accumulate LDs without oleic acid treatment. **(I)**

813 Live cell staining of WT, Vmp1, Tmem41b, and double KO ESCs with BODIPY. Scale
814 bar: 20 µm **(J)** The number of LDs per cell is plotted for all KO clones. Data are
815 represented as mean ± SD. **(K)** Double KO ESCs present an increased amount of LD
816 visualized through refractive index microscopy (top) and co-stained with BODIPY.
817
818 **Figure 2. Double KO ESCs specify all germ layers, but not the primitive**
819 **endoderm**
820
821 **(A)** Schematic representation of an Embryonic Body (EB) which consists of 3 different
822 lineages. The ectoderm expresses Fgf5 and Sox1 (grey), the mesoderm Actc1 and
823 Brachyury (blue), and the endoderm by Gata6. The surrounding region of the EB
824 corresponds to the primitive endoderm (green) and is marked by Gata6 and Dab2
825 expression. **(B)** ESCs differentiated to EBs express lineage markers for ectoderm
826 (Fgf5), mesoderm (Brachyury), endoderm (Gata6), and primitive endoderm (Dab2).
827 Graphs show mRNA levels of WT EBs normalized to the Sdha gene. Dots represent
828 biological independent experiments. Data are represented as mean ± SD. **(C)** Double
829 KO ESCs specifically show defects in expressing the primitive endoderm marker,
830 Dab2. qPCR analysis for Sox1, Actc1, and Dab2 mRNA expression in mutant EBs
831 relative to WT EBs. Two independent clones were analyzed per cell line. Each dot
832 represents an independent experiment. Data are represented as mean ± SD**.** The line
833 at 0,7 indicates an arbitrary threshold after which successful expression of the marker
834 is considered. Statistical significance (Welch's t test) is denoted as follows: ns: $p > 0.05$,
835 *: $p < 0.05$, **: $p < 0.01$, ***: $p < 0.001$. **(D-F)** Double mutant EBs show decreased
836 expression of endoderm markers. Immunofluorescence images of EB sections stained
837 for the endoderm markers GATA4 and SOX17 **(D)**, GATA6 **(E)**, DAB2 **(F)**. WT in the
838 top panel, two independent clones for Double KO condition in the center and bottom
839 panels. Nuclei are stained with Dapi. Scale bar: 50 µm.
840
841 **Figure 3. XEN differentiation in Double KO cells is delayed(A-B)**
842
843 Double KO ESCs show a delay in XEN differentiation. **(A)** Brightfield images of XEN
844 cells at day 6 of differentiation in WT and Double KO cells. XEN islands are circled in
845 white in the Double KO condition. Scale bar: 100 µm. **(B)** Immunofluorescence images
846 of day 6 XEN cells stained for SOX17 and GATA4. Nuclei are stained with Dapi, Scale

847 bar: 150 µm. **(C-F)** Transcriptional analysis of XEN cells. **(C)** Differentially expressed
848 genes between Double KO and WT cells at day 2 during XEN specification. XEN
849 markers are labeled in red; differentially expressed genes in blue. **(D-E)** GO-Term
850 analysis of differentially expressed genes between Double KO and WT conditions in
851 ESCs and XEN cells in the context of developmental processes **(D)** and signaling
852 pathways **(E)**. Dot size corresponds to the number of differentially regulated genes.
853 **(F)** WNT pathway-related genes differentially expressed in Double KO cells. Heatmap
854 shows min to max expression of the average of three biological replicates for WT and
855 Double KO XEN cells. **(G-H)** VMP1 and Tmem41b depletion promotes the increase of
856 DDIT3 protein levels. **(G)** Western Blot analysis of DDIT3 expression in WT and
857 Double KO cells differentiated to XEN cells for 2 days. HSP90 is shown as loading
858 control. **(H)** Quantification of increased DDIT3 protein levels in three biological
859 replicates. Expression relative to WT XEN cell and normalized to respective HSP90
860 expression. Data are represented as mean ± SD. **(I)** DDIT3 silencing does not restore
861 XEN specification in Double KO cells. qPCR analysis at day 3 of differentiation for
862 Ddit3, Gata4, and Dab2 mRNA expression in mutant cells relative to WT ESCs
863 transfected without and with Ddit3 siRNA. Data are represented as mean ± SD (n=3).
864
865
866 **Figure 4. Vmp1 and Tmem41b mutant ESCs show reduced plasma membrane**
867 **abundance of the WNT receptor FZD2**
868
869 **(A)** Differences in the abundance of plasma membrane proteins in WT and VMP1^{KO}
870 cells. Volcano plot displaying differentially expressed proteins at the plasma
871 membrane in WT and VMP1^{KO} ESCs. Proteins with the most significant divergence
872 are highlighted in red. Gray lines denote the selection criteria: an absolute log2 fold-
873 change > 1 and a false discovery rate < 0.05. The position of FZD2 is annotated. **(B)**
874 GO term analysis of proteins differentially abundant at the plasma membrane of WT
875 and Vmp1^{KO} cells. Shown are GO terms related to protein localization and molecular
876 function. **(C)** Abundance of Frizzled receptors identified by MS analysis in WT and
877 mutant cells. The average and standard error is reported for three independent
878 biological replicates **(D)** Western blot analysis of HA-FZD2 abundance at the PM in
879 WT, VMP1^{KO}, and Double KO ESCs. E-CADHERIN and ACTIN serve as controls for
880 PM purification and loading, respectively. **(E)** Quantification of HA-FZD2 protein levels

881 at the PM across three biological replicates relative to WT cells and normalized to the
882 total HA-FZD2 (Input). Data are represented as mean ± SD. **(F)** Western blot analysis
883 of HA-FZD2 abundance at the PM in WT and Double KO cells differentiated into XEN
884 cells for 2 days.
885
886 **Figure 5. Activation of WNT signaling rescues the delay of Double KO cells in**
887 **XEN differentiation**
888
889 **(A)** Cytoplasmic β-CATENIN levels are reduced in Double KO cells. Western blot
890 analysis was performed on whole-cell lysates (1/50) and purified cytoplasmic fractions
891 (1/50) from WT and Double KO cells. E-CADHERIN, Histone H3, and ACTIN were
892 used as controls for purification and loading. Whole-cell and purified cytoplasmic
893 fractions are shown with the same exposure conditions. **(B)** Chiron-dependent WNT
894 activation rescues the delay of Double KO XEN differentiation. IF staining for SOX17
895 and GATA4; nuclei are stained with Dapi. Scale Bar: 150 µm. **(C-D)** FZD2
896 overexpression rescues the differentiation delay in Double KO XEN cells. **(C)**
897 Immunofluorescence staining for SOX17 and GATA4 in WT and Double KO cells.
898 Nuclei are counterstained with DAPI. Scale bar: 100 µm. **(D)** Quantification of GATA4
899 and SOX17 positive cells during XEN differentiation, expressed as a percentage of
900 total cells (DAPI-stained).
901

Figure1

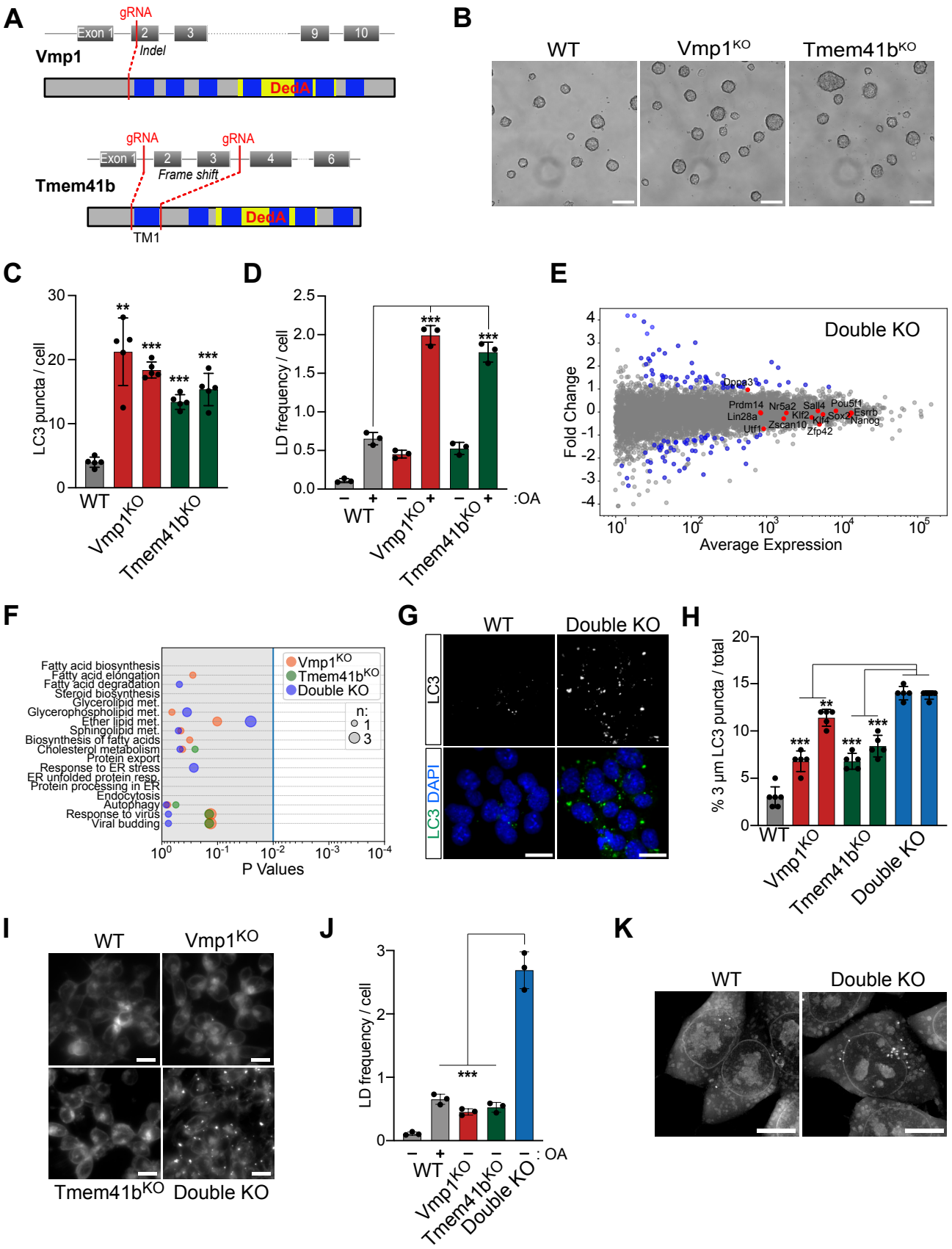
A
gRNA
Exon 1
2
3
9
10
Indel
Vmp1
DedA
gRNA
gRNA
Exon 1
2
3
4
6
Frame shift
Tmem41b
DedA
TM1
B
WT
Vmp1KO
Tmem41bKO
C
LC3 puncta / cell
WT
Vmp1KO
Tmem41bKO
D
LD frequency / cell
:OA
WT
Vmp1KO
Tmem41bKO
E
Double KO
Fold Change
Average Expression
Dppa3
Prdm14
Nr5a2
Sall4
Pou5f1
Lin28a
Klf2
Esrrb
Zscan10
Utf1
Klf4
Sox2
Nanog
Zfp42
F
Fatty acid biosynthesis
Fatty acid elongation
Fatty acid degradation
Steroid biosynthesis
Glycerolipid met.
Glycerophospholipid met.
Ether lipid met.
Sphingolipid met.
Biosynthesis of fatty acids
Cholesterol metabolism
Protein export
Response to ER stress
ER unfolded protein resp.
Protein processing in ER
Endocytosis
Autophagy
Response to virus
Viral budding
Vmp1KO
Tmem41bKO
Double KO
n:
1
3
P Values
G
WT
Double KO
LC3
LC3 DAPI
H
% 3 µm LC3 puncta / total
WT
Vmp1KO
Tmem41bKO
Double KO
I
WT
Vmp1KO
Tmem41bKO
Double KO
J
LD frequency / cell
:OA
WT
Vmp1KO
Tmem41bKO
Double KO
K
WT
Double KO

Figure 2

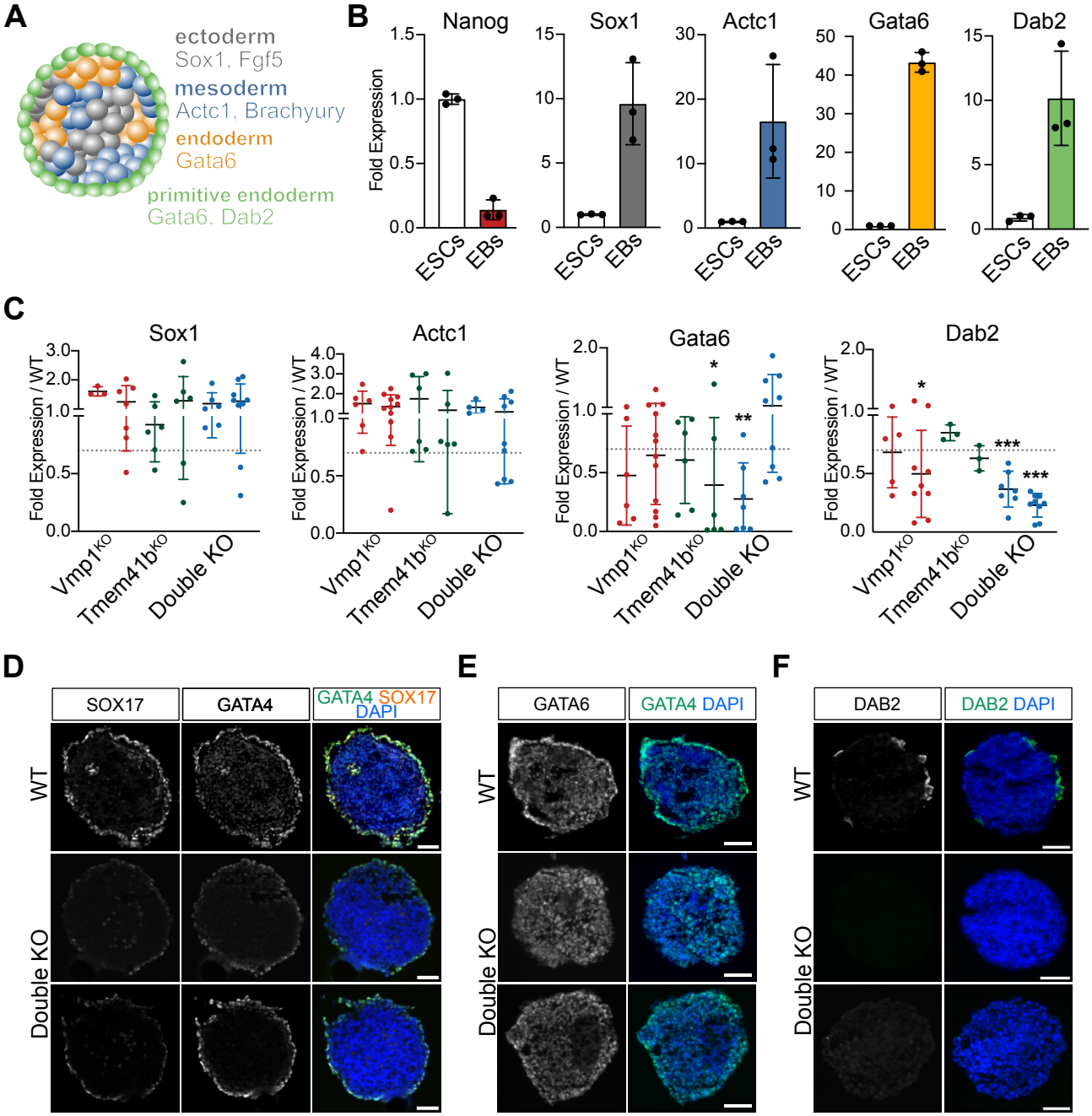
A
ectoderm
Sox1, Fgf5
mesoderm
Actc1, Brachyury
endoderm
Gata6
primitive endoderm
Gata6, Dab2
B
Nanog
Sox1
Actc1
Gata6
Dab2
Fold Expression
ESCs
EBs
C
Sox1
Actc1
Gata6
Dab2
Fold Expression / WT
Vmp1KO
Tmem41bKO
Double KO
D
SOX17
GATA4
GATA4 SOX17 DAPI
WT
Double KO
E
GATA6
GATA4 DAPI
F
DAB2
DAB2 DAPI

Figure 3

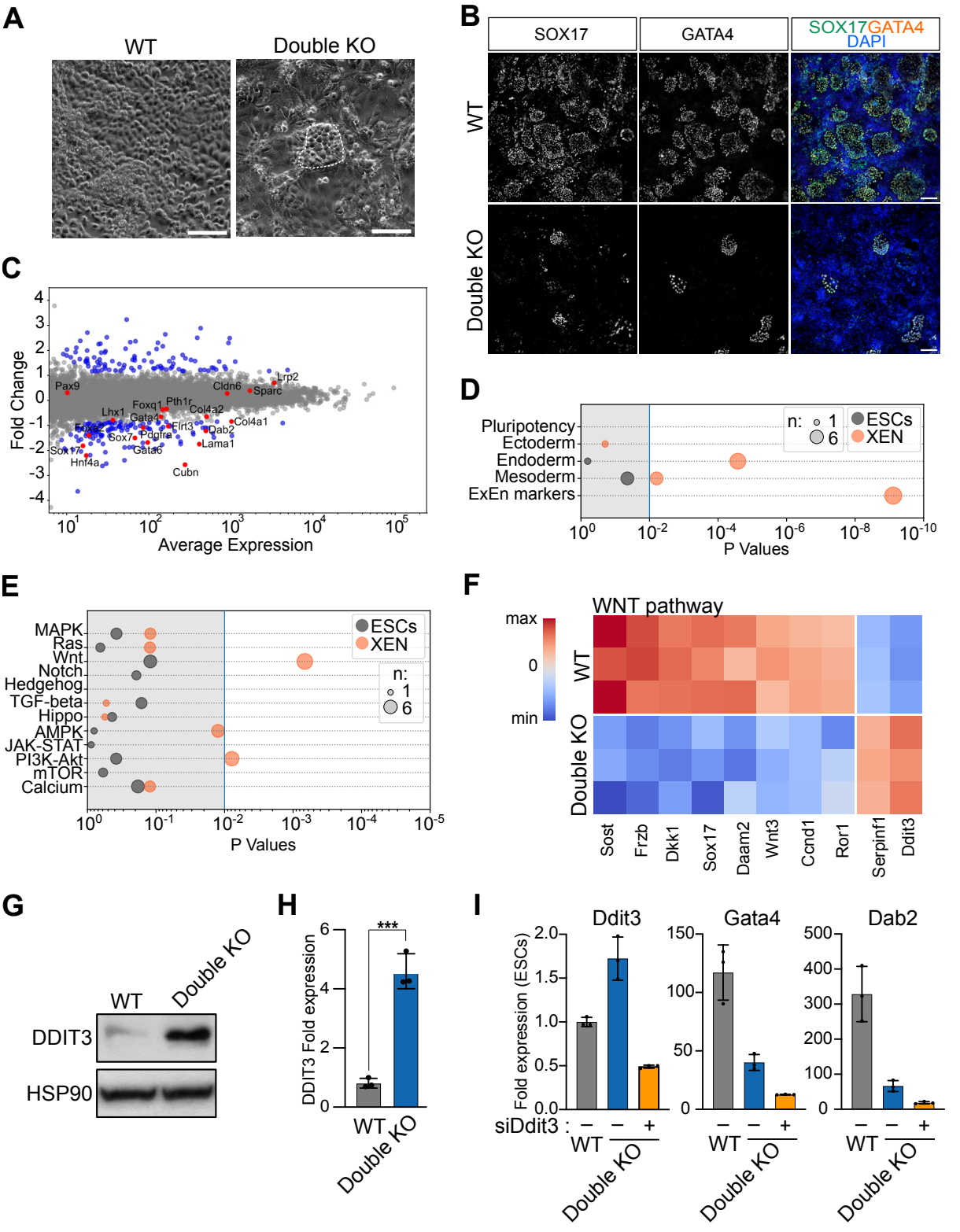
A
WT
Double KO
B
SOX17
GATA4
SOX17GATA4
DAPI
WT
Double KO
C
Fold Change
Average Expression
Pax9
Lhx1
Foxq1
Pth1r
Gata4
Col4a2
Cldn6
Sparc
Lrp2
Col4a1
Flrt3
Dab2
Lama1
Pdgfra
Sox7
Gata6
Sox17
Hnf4a
Cubn
D
Pluripotency
Ectoderm
Endoderm
Mesoderm
ExEn markers
n: 1 6
ESCs
XEN
P Values
E
MAPK
Ras
Wnt
Notch
Hedgehog
TGF-beta
Hippo
AMPK
JAK-STAT
PI3K-Akt
mTOR
Calcium
ESCs
XEN
n: 1 6
P Values
F
WNT pathway
max
0
min
WT
Double KO
Sost
Frzb
Dkk1
Sox17
Daam2
Wnt3
Ccnd1
Ror1
Serpinf1
Ddit3
G
WT
Double KO
DDIT3
HSP90
H
DDIT3 Fold expression
***
WT
Double KO
I
Ddit3
Gata4
Dab2
Fold expression (ESCs)
siDdit3 : – – +
WT
Double KO

Figure 4

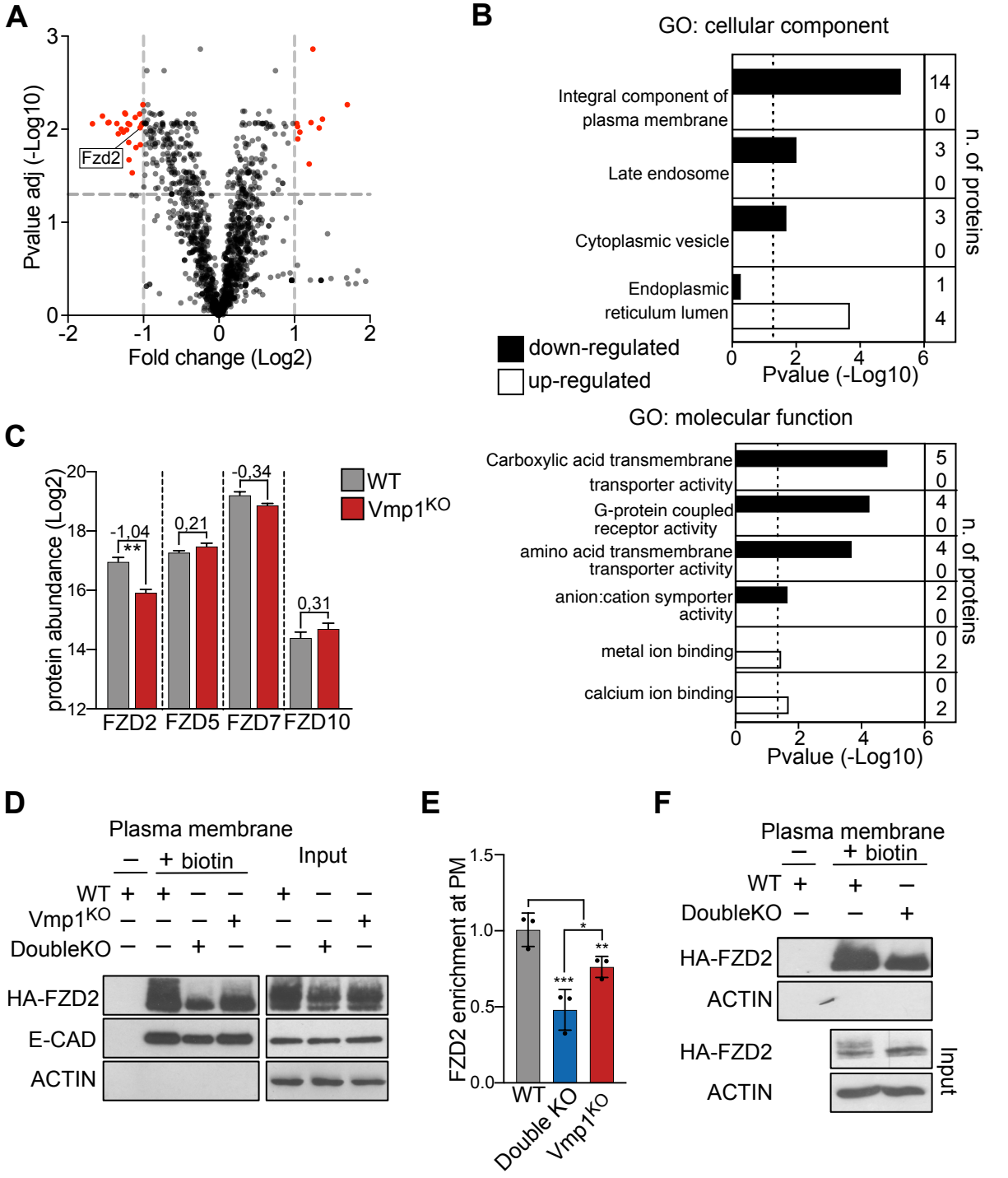
A
Pvalue adj (-Log10)
Fold change (Log2)
Fzd2
B
GO: cellular component
Integral component of plasma membrane
Late endosome
Cytoplasmic vesicle
Endoplasmic reticulum lumen
n. of proteins
down-regulated
up-regulated
Pvalue (-Log10)
GO: molecular function
Carboxylic acid transmembrane transporter activity
G-protein coupled receptor activity
amino acid transmembrane transporter activity
anion:cation symporter activity
metal ion binding
calcium ion binding
C
protein abundance (Log2)
WT
Vmp1KO
-1,04
0,21
-0,34
0,31
FZD2 FZD5 FZD7 FZD10
D
Plasma membrane
+ biotin
Input
WT
Vmp1KO
DoubleKO
HA-FZD2
E-CAD
ACTIN
E
FZD2 enrichment at PM
WT
Double KO
Vmp1KO
F
Plasma membrane
+ biotin
WT
DoubleKO
HA-FZD2
ACTIN
Input

Figure 5

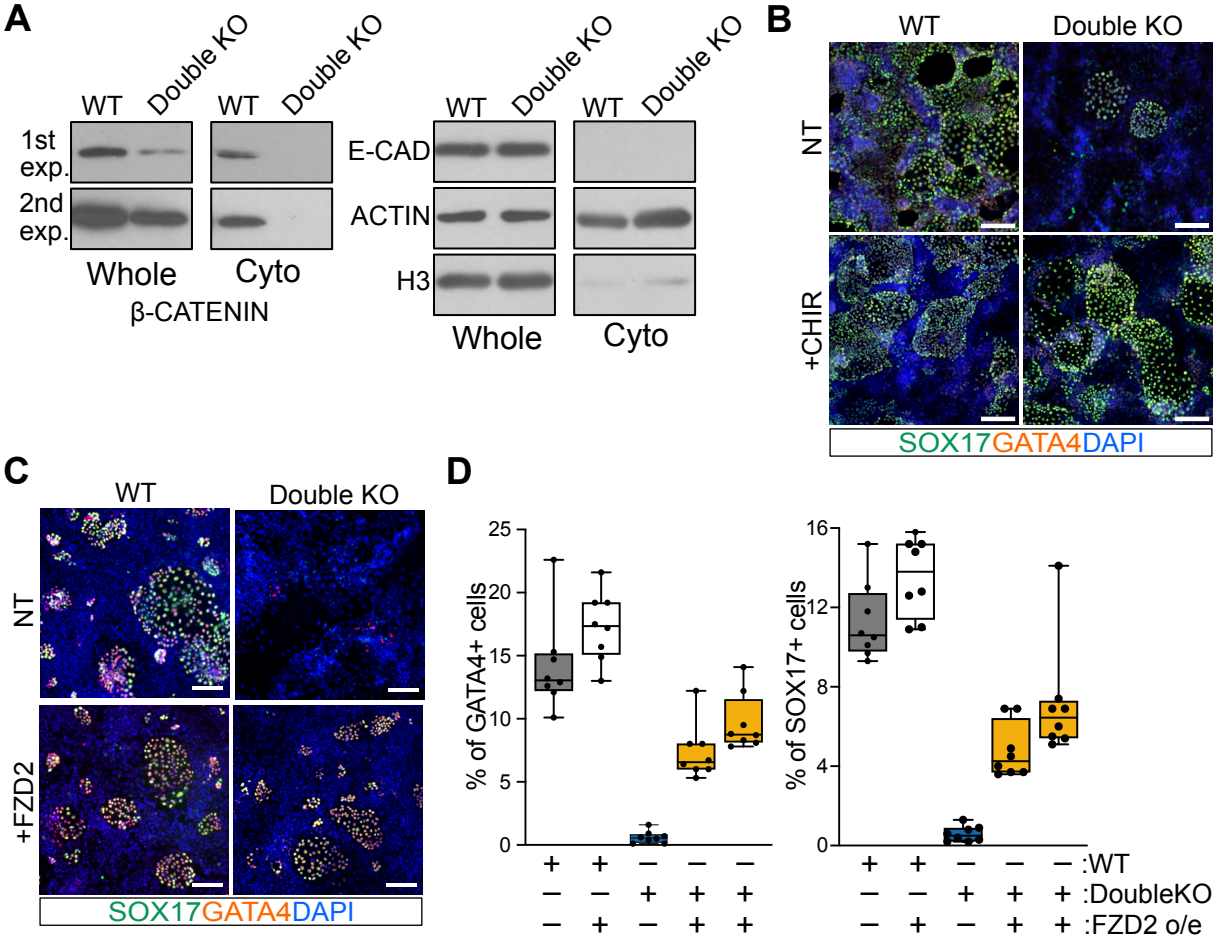
A
WT
Double KO
WT
Double KO
1st exp.
2nd exp.
Whole
Cyto
β-CATENIN
WT
Double KO
WT
Double KO
E-CAD
ACTIN
H3
Whole
Cyto
B
WT
Double KO
NT
+CHIR
SOX17GATA4DAPI
C
WT
Double KO
NT
+FZD2
SOX17GATA4DAPI
D
% of GATA4+ cells
% of SOX17+ cells
:WT
:DoubleKO
:FZD2 o/e